Structural, Optical, and Improved Field-Emission Properties of Tetrapod-Shaped Sn-Doped ZnO Nanostructures Synthesized via Thermal Evaporation

Xiongtu Zhou, Tihang Lin, Yuhui Liu, Chaoxing Wu, Xiangyao Zeng, Dong Jiang,[†] Yong-ai Zhang,* and Tailiang Guo*

College of Physics and Information Engineering, Fuzhou University, 350002 Fuzhou, China

[†]Center of Analysis and Test, East China University of Science and Technology, 200237 Shanghai, China

ABSTRACT: High-quality tetrapod-shaped Sn-doped ZnO (T-SZO) nanostructures have been successfully synthesized via the thermal evaporation of mixed Zn and Sn powder. The effects of the Sn dopant on the morphology, microstructure, optical, and field-emission (FE) properties of T-SZO were investigated. It was found that the growth direction of the legs of T-SZO is parallel to the [0001] crystal c-axis direction and that the incorporation of Sn in the ZnO matrix increases the aspect ratio of the tetrapods, leads to blue shift in the UV region, and considerably improves the FE performance. The results also show that tetrapod cathodes with around a 0.84 atom % Sn dosage have the best FE properties, with a turn-on field of 1.95 V/μm, a current density of 950 μA/cm^2 at a field of 4.5 V/μm, and a field-enhancement factor as high as 9556.

KEYWORDS: Sn-doped ZnO tetrapods, thermal evaporation, photoluminescence, field emission, enhancement factor
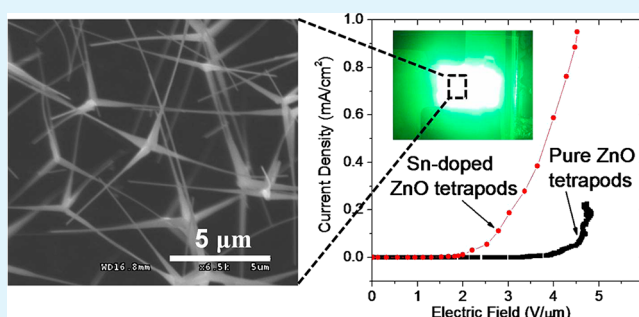
1. INTRODUCTION

Field emission (FE), also known as cold emission, is one of the main features of nanostructures and has been extensively studied for its importance in both fundamental research and device applications.[1,2] In recent years, high-performance field emitters have attracted a lot of attention because of their wide applications in FE-based vacuum microelectronic devices, such as field-emission displays, microwave, and amplifiers, where a higher current density, larger field-enhancement factor, and lower turn-on field and threshold field are needed.[3−5]

The ZnO nanostructure has been found to be potentially useful in high-quality FE devices because of its low work functions and high thermal and mechanical stability as well as high oxidation resistance in harsh environments. In particular, quasi 1D ZnO nanostructures, such as nanowires,[6] nanorods,[7] nanoneedles,[8] and nanotetrapod,[9−11] have been considered to be an ideal candidate for achieving high-FE current density at a low electric field because of their high aspect ratio. However, their relatively low conductivity has hindered their further applications in the field of efficient FE devices, so the improvement of their electron FE properties are highly desirable.[1,12] Recent research on the enhancement of FE characteristics in ZnO nanostructures mainly focused on two effective approaches: one is optimizing the geometric factor[8,13,14] by increasing the alignment and aspect ratio (height to width) or reducing the tip size of the nanostructures, and the other is increasing conductivity and reducing the work

function by selective element doping, combining with other materials, or ion implantation.[15−18]

According to previous research, the doping of ZnO with group III (Al, In, and Ga) and group IV (Sn and Pb) elements offers an effective approach to tailor the electrical properties and to improve the FE characteristics. For instance, Yang et al.[15] revealed that Al-doped ZnO nanowires with an Al dosage of 3 atom % presented superior FE characteristics to pure ZnO. Sheini et al.[16] found that a turn-on field as low as 0.68 V/μm can be obtained in 0.5 atom % Sn-doped ZnO nanowires, and they attributed this superior field-emission behavior to the higher photoconductivity. Ahmad et al.[18] reported a high field-enhancement factor of 9490 ± 2 for In-doped ZnO nanowires.

However, among the family of ZnO nanoscale materials, the tetrapod-shaped ZnO (T-ZnO) nanostructure is a unique structure and has displayed many distinct and promising applications, such as in field emission,[19] self-reporting materials (stress sensitive photoluminescence),[20,21] fluorescent stress probes,[22] and polymers linkers.[23] In particular, when used as field emitters, the four legs yield more efficient electron emission and there is always one leg vertically oriented to the anode, enabling a lower turn-on field.[19] As elucidated above, both external causation and internal features are crucial to the FE properties of materials. Thus, the tetrapod-shaped Sn-doped
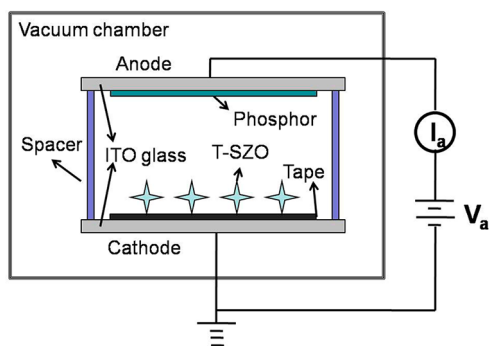
ZnO (T-SZO) nanostructures offer not only the geometric factors but also higher conductivity, which could be expected to result in a lower turn-on field and higher emission current. Nevertheless, the fabrication of T-SZO has not yet been well investigated to date, and their FE characteristics remains to be explored. In the present study, high-quality T-SZO with various dosages of Sn were successfully synthesized via the thermal evaporation of mixed Zn and Sn powders, and the influences of the Sn dopant on the photoluminescence (PL) and FE properties were investigated.

2. EXPERIMENTAL METHODS

2.1. Synthesis of T-SZO Nanostructures. The fabrication of T-SZO was carried out in a horizontal quartz tube furnace, where the temperature can be well controlled. First, the furnace was heated at a rate of 30 °C/min, and the temperature was maintained at 950°C. A crucible was then placed at the center position of the tube for preheating. Once the furnace temperature became stable, the crucible was pulled out to near the inlet of the tube, and a mixture of Zn and Sn (99.99%, Aldrich) powders was poured into it by an iron spoon followed immediately by pushing the crucible back into the central region of the quartz tube furnace using long crucible tongs. The atomic ratio of the Sn dopant in the mixture was controlled as 0 (undoped, Sn0), 1 (Sn1), 3 (Sn3), 5 (Sn5), 10 (Sn10), and 15 atom % (Sn15), respectively. The reactions were kept at the temperature of 950 °C for 90 s, and the crucible containing the T-SZO was then taken out and placed at room temperature for natural cooling. Afterwards, the white products were collected for characterization.

2.2. Characterization of T-SZO Nanostructures. The morphology of the synthesized products was characterized by scanning electron microscopy (SEM, Hitachi, S3000N). The crystal structure of the samples was characterized by high-resolution transmission electron microscopy (HRTEM, JEOL JEM-2010) and by X-ray diffraction (XRD, X'Pert Pro MPD) with the incident radiation of Co Kα (i.e., λ = 0.179 nm). The composition and chemical bonding states of T-SZO nanostructures were analyzed by X-ray photoelectron spectroscopy (XPS) using an ESCALab250Xi electron spectrometer (Thermo Scientific) with the incident radiation of Al Kα; the binding energies were referenced to the C 1s line at 284.8 eV of carbon. PL spectra were measured using a Hitachi F-4600 fluorescence spectrophotometer.

2.3. Preparation of T-SZO Cathode and FE Measurement. Figure 1 presents the schematic of the T-SZO cathode and the apparatus for FE measurement. First, double-sided conductive tape (<5 ohms/mm^2) with a size of ~0.8 × 1.2 mm^2 was stick on ITO glass, and the top side of the tape was paved uniformly with the white products. Subsequently, they were exposed to high-pressure air to blow away the unstuck T-SZO. The field-emission current versus the applied voltage (J−E) characteristics were measured in a planar diode configuration in a vacuum chamber evacuated to a base pressure of <2

× 10^{-5} Pa. The specimen served as a cathode, and a semitransparent phosphor screen, used as an anode, was held parallel to the cathode at a distance of ~500 μm. The measurement was reproducibly conducted more than five times.

3. RESULTS AND DISCUSSION

3.1. Morphological Characteristics. The morphology of the T-SZO growth is determined by many experimental parameters, such as gas-phase supersaturation,[24] growth temperature, and growth time.[25,26] In the present study, we kept all other experimental parameters constant and changed the concentration of the Sn dopant to tailor the effects of the Sn dopant on the morphology, microstructure, PL, and FE properties of ZnO tetrapod. It should be pointed out that the atomic ratio of Sn dopant in final ZnO tetrapods was found to be lower than that in the mixture precursors according to the XPS results (see the Results and Discussion, section 3.2). Thus, we use Sn0, Sn1, Sn3, Sn5, Sn10, and Sn15 to denote the samples in which the atomic ratio of the Sn dopant in the mixture precursors were 0 (undoped), 1, 3, 5, 10, and 15 atom %, respectively.

The synthesized T-SZO products are loose white and cottonlike, with more detailed morphology information disclosed under SEM. As illustrated in Fig. 2, all of the

Figure 2. SEM images of the ZnO tetrapods synthesized at 950 °C for 90 s with different Sn dosages. (a) Sn0, (b) Sn1, (c) Sn3, (d) Sn5, (e) Sn10, and (f) Sn15.
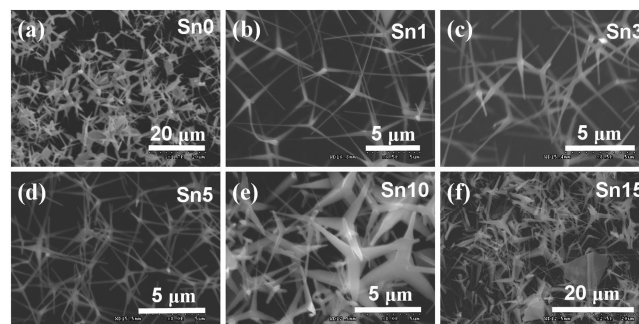
Figure 1. Schematic structure of the T-SZO cathode and the apparatus installed in a high-vacuum-chamber system for FE characteristic measurements.

synthesized T-SZO show a characteristic morphology (i.e., every individual consists of four needle-shaped or cone-shaped tetrahedrally arranged legs connected at the center, forming a tetrapod structure). Each leg is tapered, with a diameter that gradually decreases from 1 to 2 μm close to the junction of the legs down to 100−200 nm at the apex of the tip. However, different morphologies of the T-SZO tetrapods were observed with varying Sn dosages. Without Sn doping (Sn0), the product was in the form of tetrapod-shaped nanocones (Fig. 2a) accompanied with some nanosheets. The nanocones were typically 5−7 μm in length, around 1.5 μm in diameter at the junction of the legs, and had sharp tips of approximately 200 nm in diameter. With light Sn doping (Sn1−Sn5), as shown in Fig. 2b−d, the tetrapods with high purity (without other shapes) become thinner and longer, forming tetrapod-like nanoneedles with an average diameter and length of ~300 nm and ~8 μm, respectively. These tetrapod-like nanoneedles with legs of a high aspect ratio are expected to have excellent FE characteristics. When the Sn doping became heavier, the aspect ratio of the legs deteriorated again and the impurity of nanosheets increased, as shown in Figure 2e,f.
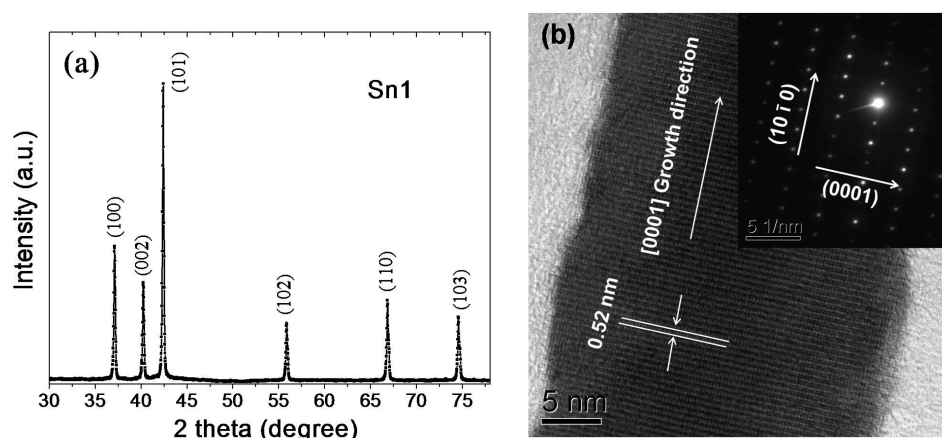
Figure 3. Microstructures of T-SZO nanomaterials: (a) XRD spectra of T-SZO nanostructure (Sn1). The XRD peak intensities are in arbitrary units (au). (b) HRTEM image of one leg for sample Sn1 and the corresponding selected-area electron diffraction (SAED) pattern (inset).
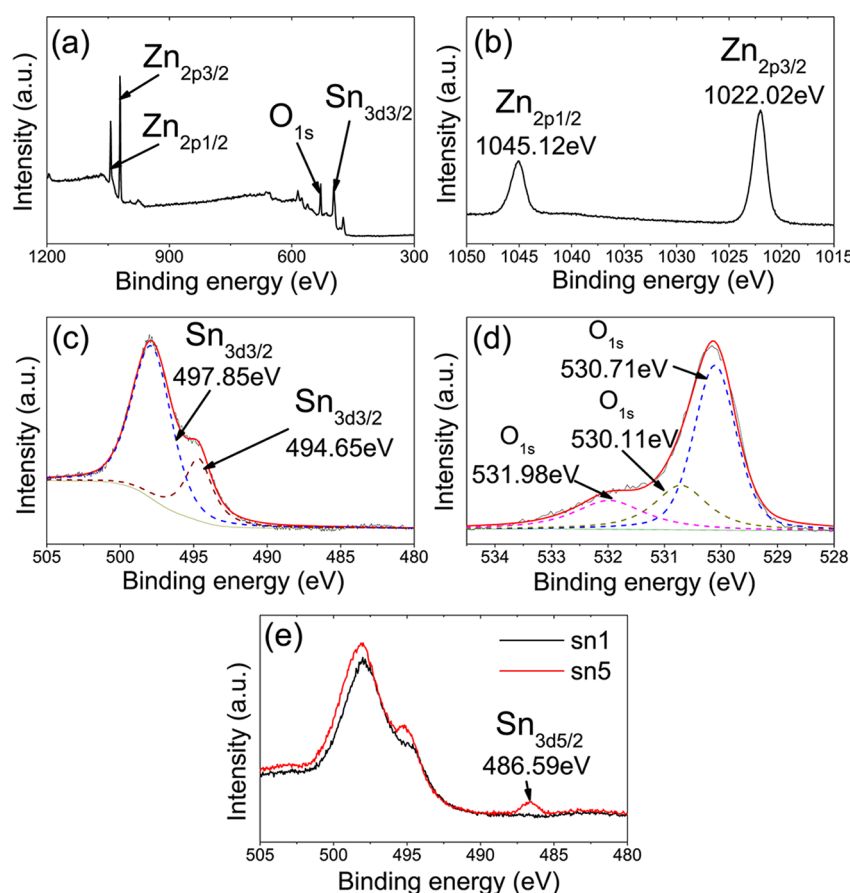
Figure 4. XPS spectra of T-SZO nanostructures: (a) survey spectrum of T-SZO nanostructures for sample Sn1, (b) high-resolution Zn 2p binding energy spectrum of Sn1, (c) Sn 3d binding energy spectrum of Sn1, (d) O 1s binding energy spectrum of Sn1, and (e) Sn 3d binding energy spectrum of both Sn1 and Sn5. All XPS peak intensities are in arbitrary units (au).

It has been commonly suggested that the formation of the ZnO-tetrapod structures originates from the octahedral multiple twins (octa-twins), which are actually ZnO nuclei formed in an oxygen atmosphere.[19,24,27] Briefly, there are two kinds of basal surfaces in the octa-twins, the Zn-(0001) surface and the O-(000$\overline{1}$) surface. The four Zn-(0001) surfaces are catalytically active and can facilitate the nucleation of ZnO species, forming the selective growth of ZnO whiskers along four [0001] directions, whereas the four O-(000$\overline{1}$) surfaces are inert and do not initiate any growth. A more detailed description of the formation mechanism of ZnO tetrapod can be found in the literature.[27] It is interesting that moderate Sn doping can raise the aspect ratio and purity of T-SZO, which is similar to that of Sn-doped ZnO nanowires.[16] However, the mechanism of the Sn-doping effects on the morphology of T-SZO is not yet clear. Under the present conditions, we attributed the evolution of the legs from nanoneedles to nanorods to a compromise between the favorable growth direction and the enhanced surface diffusion at a high growth temperature.[9]

3.2. Structural and Compositional Analysis. It was found that all of the lightly doped tetrapods (Sn0–Sn5) in this study show similar XRD spectra. Figure 3 shows a representative XRD pattern (Sn1) of the T-SZO nanostructure in which all of the major diffraction peaks can be referred to those of hexagonal wurtzite ZnO with lattice constants of a = 0.325 nm and c = 0.521 nm (JCPDS: 03-0888). It can be seen from the XRD pattern that all diffraction peaks are strong and narrow, indicating the high crystallinity of the as-synthesized T-SZO samples. Furthermore, no additional diffraction peak other than ZnO was detected, indicating that the Sn dopant might be successfully incorporated in the ZnO lattices, in the form of substitutional doping, and that the secondary-phase (e.g., SnO_2) content might be below the sensitivity of detection. These observations are similar to the results in previous reports.[9,19,24,25]

Transmission electron microscopy (TEM) was also employed to examine the microstructures of the T-SZO samples. An HRTEM image of one leg for sample Sn1 is displayed in Figure 3b, whereas the inset is the corresponding selected-area electron diffraction (SAED) pattern. The resolved lattice fringes in the HRTEM image and the clear spots of the SAED pattern reveal that the legs of the as-synthesized T-SZO nanostructures are single crystalline with spacing between two adjacent lattice fringes that is close to 0.52 nm, indicating that the growth direction of the legs is parallel to the [0001] crystal c-axis direction with little defect.

To confirm further the doping of Sn in the ZnO lattice as well as to determine the chemical composition and chemical bonding states, X-ray photoelectron spectroscopy (XPS) measurements were carried out. The obtained binding energies were corrected for the specimen charging effect by referencing the C 1s to 284.8 eV. Figure 4a presents the XPS survey of sample Sn1, showing that Zn, Sn, and O coexist in the product. The high-resolution scanning information provided in Figure 4b–d is for the separate analysis of the Zn, Sn, and O elements in T-SZO, respectively. As shown in Figure 4b, the binding energy of the Zn $2p_{3/2}$ and Zn $2p_{1/2}$ peaks located at 1022.02 and 1045.12 eV, respectively, exhibit an energy difference of 23.1 eV, which agrees well with the standard value of 22.97 eV.[26,28] However, compared to the undoped ZnO tetrapod (1021.4 and 1044.5 eV),[19] both peaks of the Zn 2p spectrum for the Sn-doped ZnO tetrapod show a small positive shift. The high-resolution XPS spectrum of Sn in Figure 4c shows a doublet corresponding to Sn $3d_{3/2}$. After multipeak Gaussian fitting, the peak located at 497.85 eV can be associated to substitutional Sn^{4+} in the ZnO lattice.[29,30] Although there is no evident SnO_2 signal in the XRD patterns, we speculate that the binding energy of 494.65 eV may be attributed to Sn^{4+} resulting from the SnO_2 as interstitials in a small amount[31] or a heterogeneous linkage of $Zn^{2+}–O–Sn^{4+}$.[32] From Figure 4c, it is also observed that the binding energy of Sn 3d at 494.65 eV had a negative shift of 0.75 eV toward a lower binding energy compared to that of SnO_2 (495.4 eV).[33,34] Together with the positive shift of the Zn 2p binding energy, it is suggested that there might be certain electron drain from the Zn^{2+} in the oxide matrix because of the presence of Sn. This kind of binding energy shift was also observed in Sn-doped TiO_2 nanospheres.[32] Similarly, in T-SZO, the electron cloud was considered to be transferred or attracted from Zn^{2+} to Sn^{4+} (or SnO_2 interstitials) through the oxygen bridge because of the difference in electronegativity of Sn (1.96) and Zn (1.65). According to the above results, it is also confirmed that Zn^{2+} was not only substituted by Sn^{4+} but also formed SnO_2 and/or $Zn^{2+}–O–Sn^{4+}$ phases to dominate the optoelectronic properties. The high-resolution XPS spectrum of the O 1s signal can be fitted by three nearly Gaussian components centered at 530.11, 530.71, and 531.98 eV, respectively (Figure 4d). The low binding energy component centered at 530.11 eV is a result of oxidized metal ions ($O–Zn^{2+}$ and $O–Sn^{4+}$). The peak at 530.71 eV is assigned to O^{2-} ions in the oxygen-deficient regions within the ZnO matrix, whereas the peak located at 531.98 eV could correspond to the existence of weakly bound oxygen species on the surface of T-SZO.[15,16]

As the Sn dosage increased, the intensity of the Sn dopant that had been incorporated into the ZnO matrix increased. Figure 4e shows the XPS spectra of the Sn signal for samples Sn1 and Sn5, from which one can see that the intensity of both peaks located at 497.85 and 494.65 eV increased. Furthermore, another peak located at 486.59 eV appeared, which is due to the Sn $3d_{5/2}$ resulting from SnO_2.[33] From quantitative XPS analyses, the atomic ratio of Sn/Zn in T-SZO are estimated to be 0.84 and 3.40 atom % for samples Sn1 and Sn5, respectively. The XPS results proved the successful incorporation of Sn in the ZnO lattices in the form of substitutional doping, SnO_2 interstitials, or a heterogeneous linkage structure of $Zn^{2+}–O–Sn^{4+}$.

3.3. Photoluminescence. To investigate the effects of Sn incorporation in the ZnO lattice on the native point defects and optical properties of T-SZO nanostructures, the photoluminescence (PL) spectrum was measured at room temperature under an excitation wavelength of 320 nm. It was found that the PL spectra contain a more narrow ultraviolet (UV) emission located near the position of 382 eV and a widened emission band centered at around 500 eV. In general, the UV emission is due to the near band-edge emission (NBE), and the emission in the visible region could be induced by deep level emission (DLE) as a result of the presence of structural defects (e.g., oxygen vacancies and SnO_2 interstitials), which is also commonly referred to as green emission.[35,36] Figure 5 gives a typical PL spectrum from sample Sn1. Notice that the DLE is intense because of the remarkable surface structural defects.[37] Indeed, the thermal evaporation is a volcanic process, and the
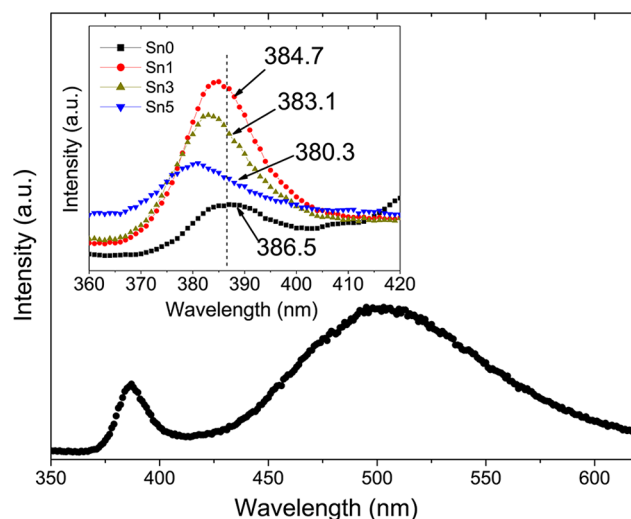
Figure 5. Room-temperature PL emission spectra of T-SZO nanostructures (Sn1). The inset shows the comparison of the UV emissions with different Sn dosages.

10070

dx.doi.org/10.1021/am4026246 | ACS Appl. Mater. Interfaces 2013, 5, 10067–10073
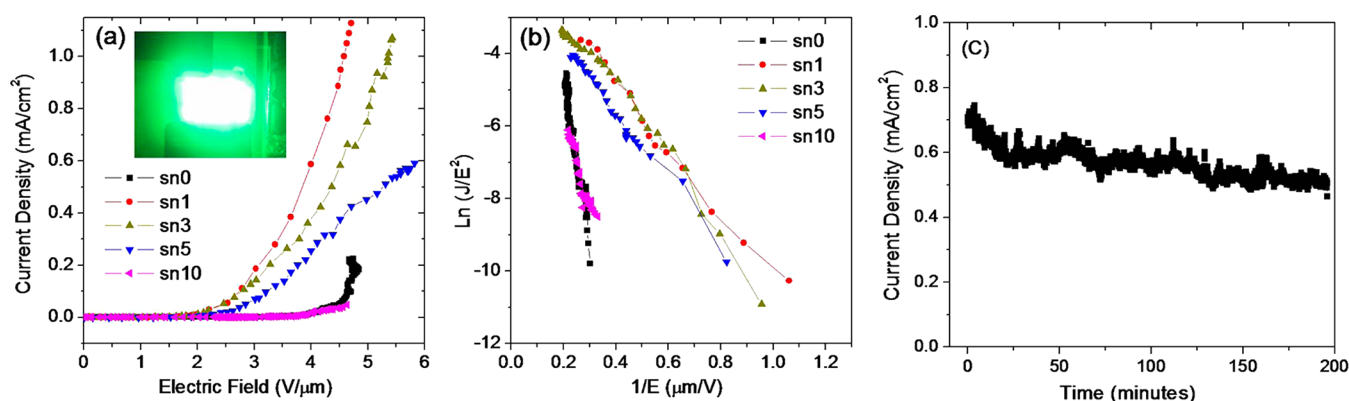
Figure 6. Field emission from T-SZO nanostructures: (a) field-emission current density applied electric field ($J-E$) characteristics. The inset shows the field-emission micrograph of sample Sn1. (b) Fowler−Nordheim (F−N) plot of the corresponding $J-E$ curves. (c) Field-emission current density of sample Sn1 under an applied electric field of 4 V/μm.

amount of oxygen is limited, which might result in a lot of oxygen deficiency in the T-SZO structure, as is also indicated in the XPS results. In addition, the UV emission peak position of Sn-doped tetrapods shows a blue shift compared with that of undoped sample, as shown in the inset of Figure 5, which is attributed to the shift of the optical band gap in Sn-doped tetrapods, as reported.[18,38] More electrons has been provided by the Sn dopants and more energy levels at the bottom of the conduction band have been taken up. During excitation, more excitons after attaining energy move to higher energy levels at the bottom of the conduction band, leading to a blue shift of the UV peak after radiative recombination. With an increase in the Sn-doping concentration, the electrons that have taken up the conduction band increase, leading to a more and more obvious blue shift of the UV emission peak. Our results agree well with previous reports.[18,39]

3.4. Field Emission. To evaluate the FE properties of the T-SZO nanostructures, T-SZO cathodes were prepared and measured. The curves of the current density J versus the applied electric field E, measured under the same conditions (d = 500 μm) as from the T-SZO cathodes, are depicted in Figure 6a. A homogeneous and bright luminescence was observed over the whole field-emission surface, as shown in the inset. The turn-on field (E_{to}) and the threshold field (E_{thr}) were defined as the field required to draw an emission current density of 10 μA/cm^2 and 1 mA/cm^2, respectively. It was found that the E_{to} for samples of Sn0, Sn1, Sn3, Sn5 and Sn10 are 3.91, 1.95, 1.96, 2.27, and 3.84 V/μm, respectively. With a further increase of the applied voltage, the emission current increases quickly. The E_{thr} for samples Sn1 and Sn3 are approximately 4.58 and 5.35 V/μm, respectively. The highest current density obtainable within our study was around 1.13 mA/cm^2 for sample Sn1 at an applied electric field of 4.71 V/μm, which is obviously higher than that of undoped TZO and samples with heavy Sn doping. It is obvious that lightly doping Sn in the ZnO tetrapods considerably improves the field-emission performance. Within our studies, sample Sn1 has the best FE performance, with the lowest turn-on field of 1.95 V/μm and the highest J at the same E value.

The $J-E$ characteristics of the samples were further analyzed according to the Fowler−Nordheim (F−N) equation, which can be described simply as follows[9]

$$J = A\left(\frac{\beta^2 E^2}{\varphi}\right)\exp\left(\frac{-B\varphi^{3/2}}{\beta E}\right) \tag{1}$$

$$\ln\left(\frac{J}{E^2}\right) = \ln\left(\frac{A\beta^2}{\varphi}\right) + \left(\frac{-B\varphi^{3/2}}{\beta}\right)\frac{1}{E} \tag{2}$$

where J denotes the current density (A/m^2), E is the applied field, A = 1.54 × 10^{-10} (A V^{-2} eV), B = 6.83 × 10^9 (V m^{-1} eV$^{-3/2}$), and Φ is the work function, which is about 5.4 eV for ZnO.[18,40] β is the field-enhancement factor, which reflects the ability of the emitters to enhance the local electric field and can be calculated from the F−N plot via calculating the slope of $\ln(J/E^2)$ versus $1/E$. The F−N plots of the emission current for T-SZO devices are demonstrated in Figure 6b, from which one can find that these curves exhibit an approximately linear dependence at high applied fields, indicating that the emitting electrons might be mainly induced by barrier tunneling electrons extracted under the electric field and would be formulated by the F−N theory. It should be pointed out that although the F−N theory is valid for a single emitter with a well-defined geometry it should also be applicable for emitters with multiple emission tips presented in this experiment, where the emission is homogeneous under high applied fields and could be regarded as an average effect of all emission tips. Thus, the β of T-SZO devices could be estimated from the average slope of the F−N plot to be about 1919, 9556, 9256, 8938, and 3614 for samples of Sn0, Sn1, Sn3, Sn5 and Sn10, respectively. The obtained value of Sn1 is much higher than that of undoped sample (Sn0) and is comparable to the values of In doped ZnO nanowires (9490) recently reported by other groups.[18] The stability of field emitters is another important issue that is closely related to their potential applications. Figure 6c shows the emission current density versus time for sample Sn1 over a period over 200 min measured at room temperature under an applied electric field of around 4 V/μm. The current density is stable, with slight fluctuations that may be due to ion bombardment during the emission process.[17]

The overall FE performance of Sn-doped ZnO nano-tetrapods (i.e., turn-on fields and β factor) is superior to that of pure ZnO nanotetrapods. The lower turn-on field for Sn-doped ZnO nanotetrapods can be attributed to an Sn-dopant induced increase in electrons in the conduction band, as was also discussed in the PL performance. According to F−N theory, the β factor is strongly dependent on the geometric

structure, including the geometry shape, size, aspect ratio, tapering, alignment, and uniformity.[16,41,42] The higher β factor of the Sn-doped ZnO nanotetrapods in this study might be attributed predominantly to their higher aspect ratio. Although the Sn dopant induced more electrons in the conduction band with increased Sn dosage, as revealed by PL investigation, the aspect ratio decreased when the Sn dosage was higher than that of sample Sn1, as can be seen from the SEM results. Thus, we obtained the best FE performance for sample Sn1, whose atomic ratio of Sn/Zn is around 0.84 atom %. The results of the SEM, XRD, PL, and FE dovetail well with each other, showing the high performance of T-SZO nanostructures obtained in the present study, which is expected to find potential applications in the field of vacuum microelectronic devices.

4. CONCLUSIONS

High-quality tetrapod-like Sn-doped ZnO (T-SZO) nanostructures have been successfully synthesized via the thermal evaporation of mixed Zn and Sn powder. The Sn-doped ZnO tetrapods exhibit four legs with a high aspect ratio and sharp tips. The current density has been significantly increased from 496 to 950 μA/cm^2 under the same electric field of 4.5 V/μm, and the enhancement factor increases from 1919 to 9556 via 0.84 atom % Sn doping. The results of the XRD, TEM, PL, and FE data dovetail well with each other, revealing that the excellent FE behavior of T-SZO is governed by the high aspect ratio of the legs in the unique tetrapod-like structures and that the Sn dopant induced more electrons in the conduction band for the Sn-doped ZnO nanotetrapods.

■ AUTHOR INFORMATION

Corresponding Authors
*E-mail: calmeloin@126.com (Y.Z.). Tel: +86 591 87893299. Fax: +86 591 87892643.
*E-mail: gtl_fzu@hotmail.com (T.G.).
Notes
The authors declare no competing financial interest.

■ ACKNOWLEDGMENTS

■ REFERENCES

(1) Zhai, T. Y.; Li, L.; Ma, Y.; Liao, M. Y.; Wang, X.; Fang, X. S.; Yao, J. N.; Bando, Y.; Golberg, D. Chem. Soc. Rev. 2011, 40, 2986−3004.
(2) Gautam, U. K.; Panchakarla, L. S.; Dierre, B.; Fang, X. S.; Bando, Y.; Sekiguchi, T.; Govindaraj, A.; Golberg, D.; Rao, C. N. R. Adv. Funct. Mater. 2009, 19, 131−140.
(3) Fang, X. S.; Bando, Y.; Gautam, U. K.; Ye, C.; Golberg, D. J. Mater. Chem. 2008, 18, 509−522.
(4) Zhai, T. Y.; Fang, X. S.; Bando, Y. S.; Liao, Q.; Xu, X. J.; Zeng, H. B.; Ma, Y.; Yao, J. N.; Golberg, D. ACS Nano 2009, 3, 949−959.
(5) Ding, J. J.; Yan, X. B.; Li, J.; Shen, B. S.; Yang, J.; Chen, J. T.; Xue, Q. J. ACS Appl. Mater. Interfaces 2011, 3, 4299−4305.
(6) Rackauskas, S.; Nasibulin, A. G.; Jiang, H.; Tian, Y.; Statkute, G.; Shandakov, S. D.; Lipsanen, H.; Kauppinen, E. I. Appl. Phys. Lett. 2009, 95, 183114−183116.
(7) Kang, H. W.; Yeo, J.; Hwang, J. O.; Hong, S.; Lee, P.; Han, S. Y.; Lee, J. H.; Rho, Y. S.; Kim, S. O.; Ko, S. H.; Sung, H. J. J. Phys. Chem. C 2011, 115, 11435−11441.
(8) Pan, N.; Xue, H. Z.; Yu, M. H.; Cui, X. F.; Wang, X. P.; Hou, J. G.; Huang, J. X.; Deng, S. Z. Nanotechnology 2010, 21, 225707−225712.
(9) Ma, L. A.; Guo, T. L. Ceram. Int. 2013, 39, 6923−6929.
(10) Lee, G. H. Ceram. Int. 2011, 37, 189−193.
(11) Rackauskas, S.; Mustonen, K.; Järvinen, T.; Mattila, M.; Klimova, O.; Jiang, H.; Tolochko, O.; Lipsanen, H.; Kauppinen, E. I.; Nasibulin, A. G. Nanotechnology 2012, 23, 095502−095506.
(12) Zeng, H. B.; Xu, X. J.; Bando, Y.; Gautam, U. K.; Zhai, T. Y.; Fang, X. S.; Liu, B. D.; Golberg, D. Adv. Funct. Mater. 2009, 19, 3165−3172.
(13) Zhang, G. H.; Wei, L.; Chen, Y. X.; Mei, L. M.; Jiao. Mater. Lett. 2013, 96, 131−134.
(14) Kim, H.; Jeon, S.; Lee, M.; Lee, J.; Yong, K. J. Mater. Chem. 2011, 21, 13458−13463.
(15) Yang, P. Y.; Wang, J. L.; Tsai, W. C.; Wang, S. J.; Lin, J. C.; Lee, I. C.; Chang, C. T.; Cheng, H. C. J. Nanosci. Nanotechnol. 2011, 11, 6013−6019.
(16) Sheini, F. J.; More, M. A.; Jadkar, S. R.; Patil, K. R.; Pillai, V. K.; Joag, D. S. J. Phys. Chem. C 2010, 114, 3843−3849.
(17) Shinde, D. R.; Chavan, P.G.; Sen, S.; Joag, D. S.; More, M. A.; Gadkari, S. C.; Gupta, S. K. ACS Appl. Mater. Interfaces 2011, 3, 4730−4735.
(18) Ahmad, M.; Sun, H.; Zhu, J. ACS Appl. Mater. Interfaces 2011, 3, 1299−1305.
(19) Wan, Q.; Yu, K.; Wang, T. H.; Lin, C. L. Appl. Phys. Lett. 2003, 83, 2253−2255.
(20) Jin, X.; Gotz, M.; Wille, S.; Mishra, Y. K.; Adelung, R.; Zollfrank, C. Adv. Mater. 2013, 25, 1342−1347.
(21) Choi, C. L.; Koski, K. J.; Olson, A. C. K.; Alivisatos, A. P. Proc. Natl. Acad. Sci. U.S.A. 2010, 107, 21306−21310.
(22) Raja, S. N.; Olson, A. C. K.; Thorkelsson, K.; Luong, A. J.; Hsueh, L. L.; Chang, G. Q.; Gludovatz, B.; Lin, L. W.; Xu, T.; Ritchie, R. O.; Alivisatos, A. P. Nano Lett. 2013, 13, 3915−3922.
(23) Jin, X.; Strueben, J.; Heepe, L.; Kovalev, A.; Mishra, Y. K.; Adelung, R.; Gorb, S. N.; Staubitz, A. Adv. Mater. 2012, 24, 5676−5680.
(24) Wang, Y.G.; Sakurai, M.; Aono, M. Nanotechnology 2008, 19, 245610−245614.
(25) Lee, G. H. Ceramics International 2011, 37, 189−193.
(26) Handbook of X-ray Photoelectron Spectroscopy; Muilenbenger, G. E., Ed.; PerkinElmer Corporation: Eden Prarie, MN, 1979.
(27) Wang, Z. L.; Kong, X. Y.; Ding, Y.; Gao, P. X.; Hughes, W. L.; Yang, R. S.; Zhang, Y. Adv. Funct. Mater. 2004, 14, 943−956.
(28) Chemical Rubber Company Handbook of Chemistry and Physics, 81st ed.; Lide, D. R., Ed.; CRC Press: Boca Raton, FL, 2000.
(29) Chen, K. J.; Hung, F. Y.; Chen, Y. T.; Chang, S. J.; Hu, Z. S. Mater. Trans. 2010, 51, 1340−1345.
(30) Szuber, J.; Czempik, G.; Larcipreteb, R.; Koziej, D.; Adamowicz, B. Thin Solid Films 2001, 391, 198−203.
(31) Bae, S. Y.; Na, C. W.; Kang, J. H.; Park, J. J. Phys. Chem. B 2005, 109, 2526−2531.
(32) Li, J.; Zeng, H. C. J. Am. Chem. Soc. 2007, 129, 15839−15847.
(33) Jing, L.; Fu, H.; Wang, B.; Wang, D.; Xin, B.; Li, S.; Sun. Appl. Catal., B 2006, 62, 282−291.
(34) Teo, S. H.; Zeng, H. C. J. Phys. Chem. B 2001, 105, 9093−9100.
(35) Djurišić, A. B.; Choy, W. C. H.; Roy, V. A. L.; Leung, Y. H.; Kwong, C. Y.; Cheah, K. W.; Rao, T. K. G.; Chan, W. K.; Lui, H. F.; Surya, C. Adv. Funct. Mater. 2004, 14, 856−864.
(36) Chen, S. L.; Lee, S. K.; Chen, W. M.; Dong, H. X.; Sun, L.; Chen, Z. H.; Buyanova, I. A. Appl. Phys. Lett. 2010, 96, 033108−033110.
(37) Du, G.; Wang, J.; Wang, X.; Jiang, X.; Yang, S.; Ma, Y.; Yan, W.; Gao, D.; Liu, X.; Cao, H.; Xu, J.; Chang, R. P. H. Vacuum 2003, 69, 473−476.
(38) Chen, Y. W.; Liu, C. Y.; Lu, S. X.; Xu, C. S.; Shao, C. L.; Wang, C.; Zhang, J. Y.; Lu, Y. M.; Shen, D. Z.; Fan, X. W. J. Chem. Phys. 2005, 123, 134701−134705.

(39) Lee, S. K.; Chen, W. M.; Hongxing, D.; Chen, Z.; Buyanova, I. A. *Thin Solid Films* **2013**, *543*, 114−117.

(40) Jo, S. H.; Banerjee, D.; Ren, Z. F. *Appl. Phys. Lett.* **2004**, *85*, 1407−1409.

(41) Chang, Y. M.; Liu, M. C.; Kao, P. H.; Lin, C. M.; Lee, H. Y.; Juang, J. Y. *ACS Appl. Mater. Interfaces* **2012**, *4*, 1411−1416.

(42) Song, J. Z.; Kulinich, S. A.; Yan, J.; Li, Z. G.; He, J. P.; Kan, C. X.; Zeng, H.B. *Adv. Mater.* [Online early access] DOI: 10.1002/adma.201302293. Published Online: July 29, 2013.